

## Backbone flexibility of extended metal atom chains. Ab initio molecular dynamics for $\text{Cr}_3(\text{dpa})_4\text{X}_2$ ( $\text{X} = \text{NCS}, \text{CN}, \text{NO}_3$ ) in gas and crystalline phase

Received 00th January 20xx,  
Accepted 00th January 20xx

DOI: 10.1039/x0xx00000x

www.rsc.org/

M. Spivak,<sup>a</sup> V. Arcisauskaite,<sup>b</sup> X. López,<sup>a</sup> and C. de Graaf<sup>a,c</sup>

Recently published static DFT and CASSCF/CASPT2 calculations depicted extremely flat Potential Energy Surfaces (PES) for the Cr-Cr flexibility of  $\text{Cr}_3(\text{dpa})_4\text{X}_2$  ( $\text{X} = \text{NCS}^-, \text{CN}^-, \text{NO}_3^-$ ) extended metal atom chains (EMACs) (M. Spivak et al. *Dalton Trans.* 2017, **46**, 6202). We herein explore the thermal and crystal packing effects on the structure of EMACs using ab initio molecular dynamics (MD). Car-Parrinello DFT-based simulations of the isolated molecules show that thermal energy favors asymmetric arrangements of the  $\text{Cr}_3$  chain due, in part, to the bending of the axial ligands (X) and the increased X-Cr distance, both of which weaken  $\text{X} \rightarrow \text{Cr}$   $\sigma$ -donation. This effect is even more prominent in the crystalline phase due to the interaction between axial ligands of neighboring molecules in the unit cell. This could explain the typical discrepancies between experimental and theoretical characterization of  $\text{Cr}_3$  EMACs observed in the literature.

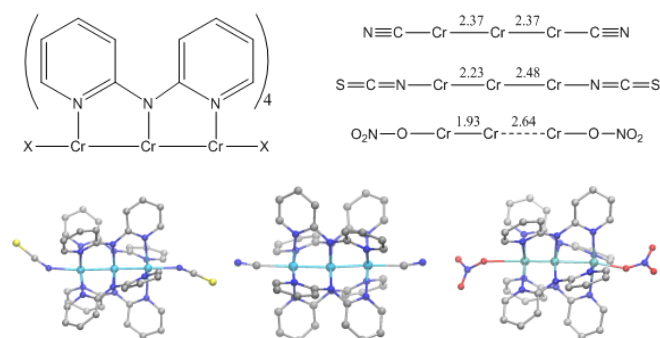


**Figure 1.** Top: Schematic representation of trichromium EMACs (left) and experimental Cr-Cr distances (Å) for  $\text{X} = \text{CN}^-$ ,  $\text{NCS}^-$  and  $\text{NO}_3^-$  axial ligands (right). Bottom: Ball and stick representation of  $\text{Cr}_3(\text{dpa})_4(\text{NCS})_2$  (left),  $\text{Cr}_3(\text{dpa})_4(\text{CN})_2$  (middle) and  $\text{Cr}_3(\text{dpa})_4(\text{NO}_3)_2$  (right). Color code: Cr (teal), N (blue), C (grey), and S (yellow). H atoms are omitted for clarity.

### Introduction

Extended Metal Atom Chain (EMAC) compounds are well-suited model systems to study the characteristics of metal-metal bonding. Furthermore, EMACs have been proposed as potential devices in molecular electronics.<sup>1-7</sup> The core of the EMACs are made of (linear) chains of up to 11 transition metals from the 1st and 2nd row of the periodic table.<sup>8-10</sup> The metal-metal interactions range from very strong, giving rise to multiple covalent bonds (Cr, Mo), to rather weak, where a description in terms of

<sup>a</sup> Departament de Química Física i Inorgànica, Universitat Rovira i Virgili, Marcel·lí Domingo 1, 43007 Tarragona, Spain.

<sup>b</sup> Department of Chemistry, Inorganic Chemistry Laboratory, University of Oxford, South Parks Road, Oxford OX1 3QR, UK.

<sup>c</sup> ICREA, Passeig Lluís Companys 23, 08010, Barcelona, Spain.

Electronic Supplementary Information (ESI) available: See DOI: 10.1039/x0xx00000x

magnetic coupling is more appropriate (Ni, Cu).<sup>11–16</sup> The resemblance with macroscopic coated wires is striking; the metal chain is held together by multichelating organic ligands, typically dipyrindylamide (dpa) or larger ligands of the same family. In addition, the chain is typically capped at both ends by inorganic ligands ( $X = \text{Cl}^-$ ,  $\text{NCS}^-$ ,  $\text{CN}^-$  or  $\text{NO}_3^-$ , among others), which not only ensure charge neutrality, but can also be used to attach the EMAC to surfaces, such as electrodes, with possible applications in molecular electronics. Moreover, axial ligands have been shown to have a non-innocent effect on the structure of the metal chain in some cases.<sup>17</sup>

Trichromium EMACs, depicted in Figure 1, form a group that survey different arrangements of Cr-Cr distances, **either all equal or asymmetrically arranged**, depending on the identity (and  $\sigma$ -donor strength) of the axial ligand.<sup>18</sup>  $\text{Cr}_3(\text{dpa})_4(\text{NCS})_2$  has been one of the most widely studied compounds in the family due to the presence of sulfur in terminal positions, allowing attachment of the molecule to gold surfaces. The experimental structure determination based on X-ray diffraction of the crystal **has been a point of debate in the literature, since the interpretation of the position of the central atom depends on the model used to refine the results. When the central ellipsoid is modelled as two positions, an asymmetric structure is obtained**: Cr-Cr distances of 2.23 and 2.48 Å, if benzene is used as crystallization solvent, and 2.22 and 2.47 Å for toluene<sup>18</sup> (Figure 1). On the other hand, Surface Enhanced Raman Spectroscopy (SERS) experiments on aqueous solutions of  $\text{Cr}_3(\text{dpa})_4(\text{NCS})_2$  adsorbed on silver nanoparticles (up to 333.15 K) suggest a symmetric structure.<sup>19</sup> The X-ray measurements on crystals with  $X = \text{CN}^-$  ( $\text{CH}_2\text{Cl}_2$  solvent) and  $\text{NO}_3^-$  ( $\text{Et}_2\text{O}$  solvent) result in symmetric (2.37 Å) and highly asymmetric (1.93 and 2.64 Å) structures, respectively.<sup>18</sup> These differences are attributed to the  $\sigma$ -donor character of the axial ligand, where stronger  $\sigma$ -donation ( $\text{CN}^- > \text{NCS}^- > \text{NO}_3^-$ ) destabilizes multiple Cr-Cr bonds, favoring symmetric arrangements.

Density functional theory (DFT) computations of the isolated molecules always favor symmetric structures irrespective of the axial ligand considered, in spite of the potential energy surface being very flat (less than 5 kcal mol<sup>-1</sup> between symmetric and asymmetric regions).<sup>20,21</sup> This symmetry issue is not just a formal question but has real consequences for the properties of the complex. Previous theoretical studies showed that symmetry distortions can increase the electrical conductance when they cause one of the orbital conduction channels to get closer to (or actually hit) the Fermi level.<sup>1,22</sup>

Knowing that systems with a large number of unpaired electrons pose a challenge to DFT—the trichromium EMACs possess twelve unpaired electrons—we have approached the structural issue from a multiconfigurational perspective.<sup>20</sup> Second-order perturbation theory based on a complete active space self-consistent field wave function (CASPT2)<sup>23–25</sup> reveals extremely flat potential energy surfaces (PES) as function of the two metal-metal distances, as well. The complex with  $\text{CN}^-$  axial ligands has a minimum for two equal Cr-Cr distances, while the asymmetric structure turns out to be slightly lower in energy for the  $\text{NO}_3^-$ -containing complex. With  $\text{NCS}^-$  in axial position, the PES shows a shallow symmetric global minimum. Hence, there is an apparent contradiction between the experimental crystal structure, the predictions of the SERS experiment and the optimal geometry

estimated from computational methods for  $\text{Cr}_3(\text{dpa})_4(\text{NCS})_2$ , which we address in the present paper.

The first point worth being considered is the theoretical description of the environment of EMACs. Determination of the experimental X-ray structure is obviously done in a crystalline phase, whereas the theoretical calculations were done with a gas phase (or vacuum) setup. This implies that crystal packing effects and other interactions with neighboring units have been so far neglected in the theoretical description. An important question in this regard is to what extent the crystal structure is relevant for a device configuration in which an isolated EMAC is attached to electrodes via the axial ligands. In such a setup, there are, in principle, no interactions with neighboring EMACs and, therefore, a structural determination in vacuum may indeed be more pertinent. Secondly, the calculations did not include any thermal effect, as standard ab initio calculations do not consider it as such, thus formally all the results refer to  $T = 0$  K. Given the flatness of the calculated PES, it should not come as a complete surprise that the Cr(II) ions are rather mobile and that a static model of the  $\text{Cr}_3$  backbone gives only a partial picture of the system. Rather than having a symmetric or an asymmetric structure, it is more likely to have a collection of different structures that average relevant properties such as the aforementioned electrical conductivity through the metal chain. For example, X-ray and SERS measurements on  $\text{Cr}_3(\text{dpa})_4\text{Cl}_2$  indicate that temperature directly affects the symmetry of the chain. Asymmetric structures are present at room temperature while symmetric ones prevail at lower temperature (15 K).<sup>11,18,19</sup>

In this work, we apply ab initio molecular dynamics (AIMD) to explore the PES of  $\text{Cr}_3(\text{dpa})_4(\text{X})_2$  with  $X = \text{NCS}^-$ ,  $\text{NO}_3^-$  and  $\text{CN}^-$  **at 300 K. In addition, we run the case of  $X = \text{NCS}^-$  at a lower temperature of 100 K for comparison.** Such simulations allow us to analyze the effect of the thermal energy on the structural flexibility of the metal chains. In the first place, we study the dynamics on one isolated unit. Next, we examine the crystal packing effects by performing MD simulations on the complete experimentally determined crystal unit cell. The starting point of these simulation runs corresponds to the available X-ray diffraction data.

## Computational Methodology

Single molecule AIMD calculations have been performed using the Car-Parrinello<sup>26</sup> approach as implemented in CPMD 3.15.<sup>27</sup> The electron density was described at the DFT/BLYP<sup>28,29</sup> level using the corresponding Troullier-Martins norm-conserving pseudopotentials and a plane wave basis set with a cut-off of 90 Ry.<sup>30</sup> Standard isotope masses were used for all the atoms except for H, which was replaced by deuterium in order to increase the time step in the dynamics (4.0 a.u. = 0.0968 fs) without losing accuracy. An orthorhombic box of dimensions 25.0 × 15.0 × 15.0 Å<sup>3</sup> was used after a series of tests to avoid interactions between the periodic replicas. The system was equilibrated at the desired temperature and then maintained at a steady temperature with a Nosé-Hoover thermostat coupling the bath to the system with frequencies of 2100 and 10000 cm<sup>-1</sup> for the ions and the electrons, respectively.<sup>31–33</sup> A fictitious electron mass of 600 a.u. was used for all the molecules, whereas the fictitious electron kinetic energy was obtained from a

preliminary annealing process. For the 300 K run, the values were 0.01810, 0.01739, 0.01909 a.u. for  $\text{NCS}^-$ ,  $\text{NO}_3^-$  and  $\text{CN}^-$  respectively. A snapshot of the nuclear positions was taken every 50 timesteps. The initial electron distribution corresponds to an up-down-up configuration of the spin moments localized at the Cr(II) ions. At some of the snapshots, we have recalculated the spin density to ensure that this electronic configuration is not lost.

Born-Oppenheimer molecular dynamics<sup>34</sup> simulations of the solid state were carried out with the VASP 5.3.<sup>35–37</sup> The projected augmented wave (PAW) formalism and plane waves with a 400 eV (29.4 Ry) cut-off were used.<sup>38,39</sup> The PAW formalism requires less stringent cut-offs than the norm conserving potentials used in the Car-Parrinello simulations. The DFT calculations to determine the electron density were performed with the PBE functional.<sup>40</sup> A time step of 0.1 fs was used at 300 K. As for the isolated molecule, the simulations are done in the NVT ensemble using the Nosé algorithm to keep the average temperature constant. The fluctuations are controlled by a Nosé mass of  $0.438 \times 10^{-27}$ ,  $0.404 \times 10^{-27}$  and  $0.187 \times 10^{-27}$  a.u. for  $\text{NCS}^-$ ,  $\text{NO}_3^-$  and  $\text{CN}^-$  respectively.

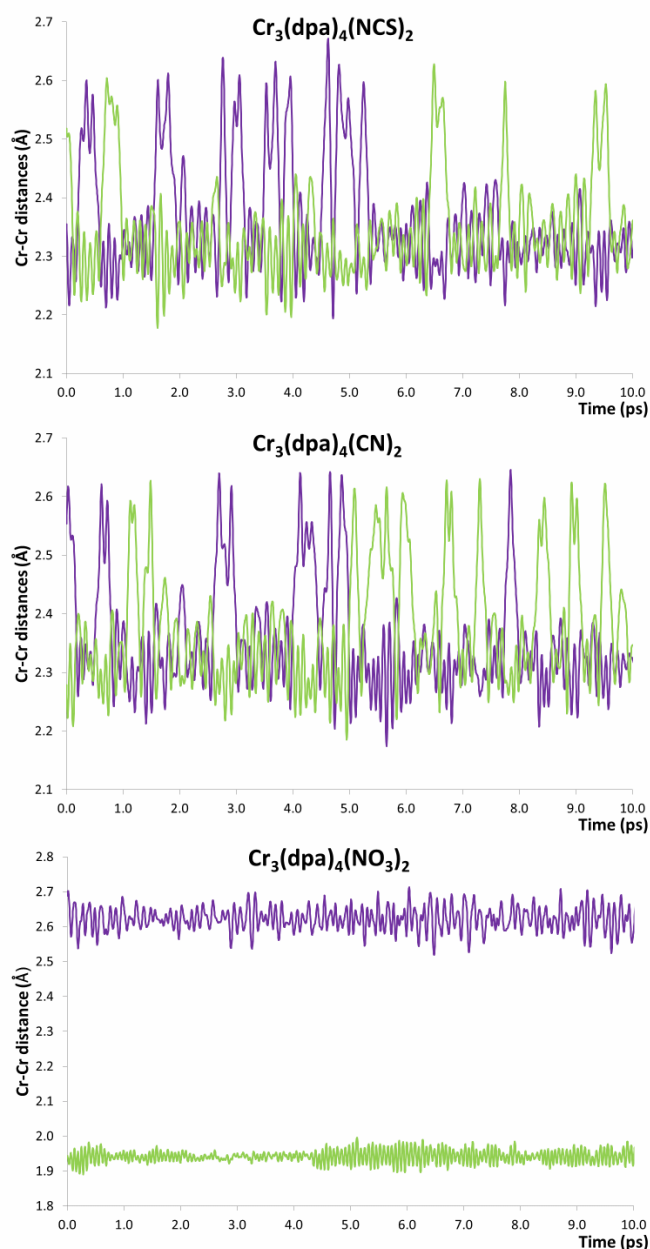


**Figure 2.** Evolution of the two Cr-Cr distances (in purple and green colour) during the molecular dynamics simulation in the gas phase at 300 K for  $\text{Cr}_3(\text{dpa})_4(\text{NCS})_2$  (top),  $\text{Cr}_3(\text{dpa})_4(\text{CN})_2$  (middle) and  $\text{Cr}_3(\text{dpa})_4(\text{NO}_3)_2$  (bottom).

## Results

### Gas Phase

We start discussing the results obtained from MD simulations for the three chromium EMACs as isolated species (see Figure 1). Recently published static calculations of the PES with the two Cr-Cr separations defining the independent variables showed in all cases relatively flat landscapes.<sup>4</sup> These results suggest that, given a certain amount of thermal energy, the central Cr moves freely,

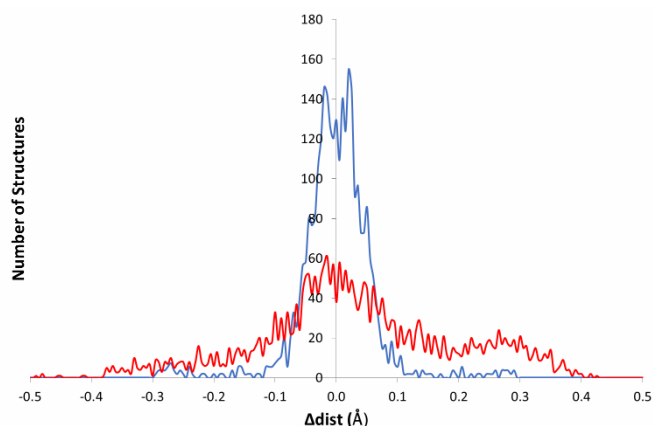


**Figure 3.** Histogram of the difference between Cr-Cr distances ( $\Delta\text{dist}$  in Å) for two different simulations of  $\text{Cr}_3(\text{dpa})_4(\text{NCS})_2$  with temperatures of 300 K (red) and 100 K (blue).

Under this hypothesis, a device configuration constructed with molecules of  $\text{Cr}_3(\text{dpa})_4(\text{NCS})_2$  would give the average conductance of a collection of structures, since these could easily interchange due to the accessible thermal energy in the experiment. Gas phase simulations are believed to be a good approximation to a device configuration, where there are no interactions between molecules and, hence, can be used to understand the electronic conductance of these and similar materials in upcoming nano-devices.

The time evolution of the two Cr-Cr distances in  $\text{Cr}_3(\text{dpa})_4(\text{NCS})_2$  during the MD run is shown in Figure 2 (top). Along the simulation, the two distances oscillate between two distinct regimes. Most of the time, the Cr-Cr distances appear close to a value of  $2.3 \pm 0.1$  Å, but in some cases one of the distances is stretched up to 2.5–2.6 Å, which is accompanied by a slight shortening of the other distance, in what appears to be a collective movement of the  $\text{Cr}_3$  backbone. This indicates that the EMAC adopts mostly a symmetric conformation but often visits regions of the PES of asymmetric nature, that is, where the difference between the two Cr-Cr distances ( $\Delta\text{dist}$ ) is larger than 0.15 Å. To quantify the balance between symmetric and asymmetric structures we plotted a histogram of  $\Delta\text{dist}$  from ca. 3000 snapshots taken along the trajectory. The red line in Figure 3 represents the histogram obtained from the simulation at 300 K. A principal distribution with two similar Cr-Cr distances can be identified ( $\Delta\text{dist} = 0.0$  Å). This set of structures ( $\Delta\text{dist} < 0.15$  Å) represents more than 70% of the total with an average Cr-Cr distance of 2.35 Å. However, there is a minor though non-negligible occurrence of unsymmetrical structures ( $\Delta\text{dist} > 0.15$  Å) with a maximum at around  $\sim 0.30$  Å. The proportion

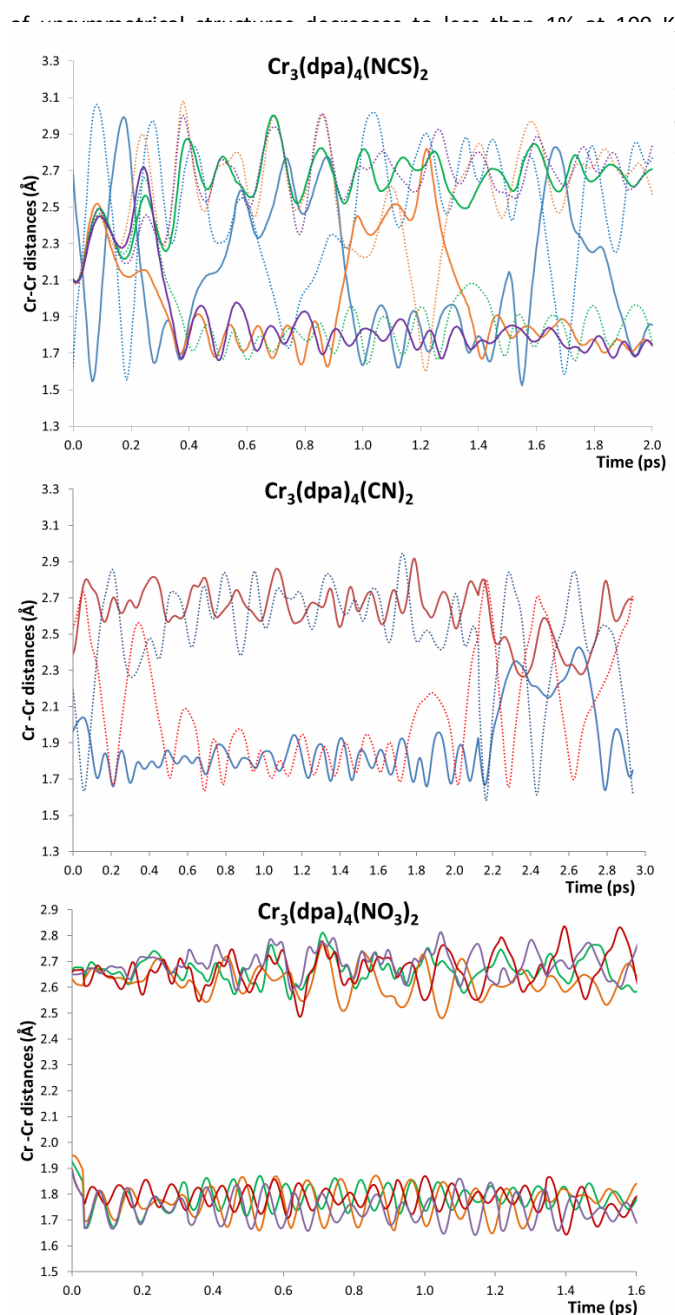


**Figure 4.** Evolution of the Cr-Cr distances during the molecular dynamics simulation of the crystalline phase at 300 K for  $\text{Cr}_3(\text{dpa})_4(\text{NCS})_2$  (top),  $\text{Cr}_3(\text{dpa})_4(\text{CN})_2$  (middle) and  $\text{Cr}_3(\text{dpa})_4(\text{NO}_3)_2$  (bottom).

The AIMD results for  $\text{Cr}_3(\text{dpa})_4(\text{CN})_2$  (Figure 2, middle) show that this system behaves similarly to the previous one. In this case, 60% of the total structures are symmetric ( $\Delta\text{dist} < 0.15 \text{ \AA}$ ) and the average Cr-Cr distance is  $2.38 \text{ \AA}$ , in agreement with previous static DFT calculations and experimental results.<sup>2, 4</sup> The similarities between  $\text{NCS}^-$  and  $\text{CN}^-$  are consistent with previous results that suggest both structures to be symmetrical, with a flat PES. This is also in agreement with SERS experiments on aqueous solutions of  $\text{Cr}_3(\text{dpa})_4(\text{NCS})_2$  (up to 333.15 K) suggesting a symmetric structure. These two ligands have a relatively strong  $\sigma$ -donor character with respect to  $\text{NO}_3^-$ . The latter, categorised as a weak donor ligand, favours an unsymmetrical arrangement of the  $\text{Cr}_3$  chain and it

should be no surprise to obtain two distinct Cr-Cr distances during the MD run. The oscillations observed in the simulation (Figure 2, bottom) are much smaller than in the previous cases, and the average values of  $1.95$  and  $2.62 \text{ \AA}$  are in excellent agreement with the experimental structure ( $1.93$  and  $2.64 \text{ \AA}$ ).

Before discussing the results of the simulations in the crystalline phase, we have to clarify first the apparent discrepancy between the prediction of a symmetric structure for  $\text{Cr}_3(\text{dpa})_4(\text{NO}_3)_2$  by standard DFT geometry optimizations and the present preference for asymmetric structures in MD simulations at 300 K. In both cases, we have used the same functional, BLYP, although actually every functional tested tends to a symmetric structure when the geometry is optimized. Furthermore, we have carefully tested the basis set, the time step and the size of the simulation box, but larger cut-offs, smaller time steps and larger boxes lead to exactly the same prominent preference for asymmetric structures in the MD calculations.

We have identified two possible reasons for the increased tendency towards asymmetric structure in MD simulations. In the first place, entropy is introduced in the theoretical description of the structures, which apparently tips the subtle balance between symmetric and asymmetric structures to the asymmetric side for the  $\text{NO}_3^-$  complex. In fact, the regular appearance of asymmetric structures in the EMACs with  $\text{CN}^-$  and  $\text{NCS}^-$  can also be ascribed to the entropy. In principle one could estimate the entropy in the static calculation by the calculation of the vibrational levels and apply the standard formulas of statistical mechanics. However, such an analysis can only be performed when the geometry corresponds to a minimum, that is, when all vibrational frequencies are positive. This can of course be done without further problems for the symmetric minimum on the PES, but we have not been able to find a fully relaxed minimum with an asymmetric  $\text{Cr}_3$  backbone. Hence, in the asymmetric geometry there will always be a vibrational mode with an imaginary eigenvalue, which makes it difficult to estimate the differential entropic effects for symmetric versus asymmetric forms.

Secondly, the averaged geometric parameters listed in Table 1 can also help to understand the preference for asymmetric structures in this case. It can be seen that the average Cr-Cr distance is significantly larger at both ends of the  $\text{Cr}_3$  chain, and the average Cr-Cr distance of the central Cr pair is further from the average value ( $2.192 \text{ \AA}$ ). This preference for asymmetric structures has been observed in previous computed static DFT calculations.

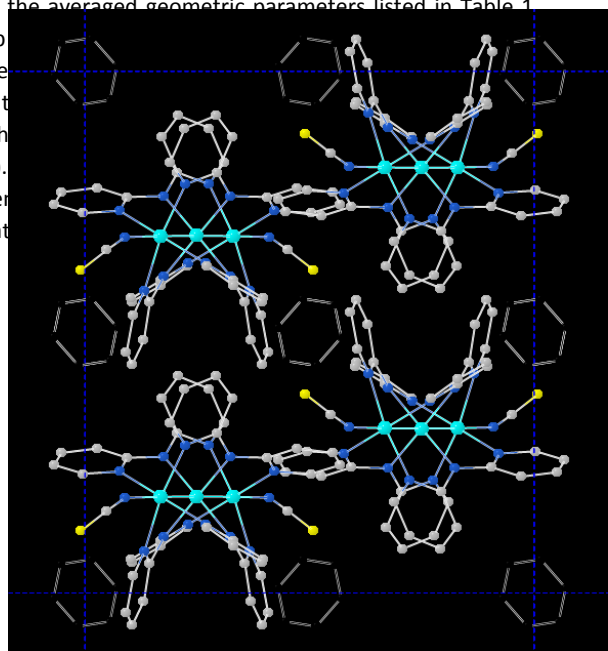


**Figure 5.** Unit cell of the  $\text{Cr}_3(\text{dpa})_4(\text{NCS})_2$  view along the  $a$  axis. Color code EMACs: Cr (teal), N (blue), C (grey) and S (yellow); Solvent: C (black). H atoms are omitted for clarity.

Cr angle is something that we did not take into consideration in previous static DFT calculations to keep  $C_2$  symmetry of the molecule. In the present dynamics, we observe the distinctive bending of the N-O-Cr angle and the computed average angles resemble the ones of the experimental structure. Such a bending could be important for the computational description of asymmetric structures as it weakens the electron density donation from the axial ligand ( $\sigma$  character), favoring the localized Cr-Cr multiple bonding as explained in previous studies.<sup>2, 4, 20</sup> Based on these results, we tested DFT optimizations of  $NCS^-$  and  $NO_3^-$  structures starting with non-linear axial angles and without imposed symmetry. We observed that linear structures are still preferred for static DFT calculations but the energy involved in the bending of the axial ligand is close in magnitude to the error of the method (1 kcal mol<sup>-1</sup>).

### Crystalline Phase

In this section, we present the results of the MD simulations in the crystalline phase for the three compounds.

For the  $NO_3^-$  system, the unit cell contains four symmetry-unique EMAC molecules and, therefore, eight Cr-Cr distances are reported. Figure 4 (bottom) shows the time evolution of these Cr-Cr distances taken from a part of the run. There are two clearly different sets of distances, one group of four distances oscillate around 2.6 Å, whereas the other four do at approximately 1.8 Å. As expected, each of the four molecules in the unit cell shows one long and one short Cr-Cr distance, and hence, the solid state dynamics is basically identical to the one in the gas phase dynamics for  $X = NO_3^-$ , indicating that the constraints imposed on the geometry by the crystal packing play little role for this complex. Finally, it is worth mentioning that the average structure is in good agreement with the experimental data ( $d(\text{Cr-Cr}) = 1.93, 2.64$  Å).

The simulation of the complex with  $CN^-$  axial ligands, represented in Figure 4 (middle), features only four Cr-Cr distances, arising from the two EMAC molecules in the unit cell. During most of the simulation time the distances oscillate around 1.8 and 2.6 Å, similar to the  $NO_3^-$  case (the average distances and angles are reported in Table S1 in the ESI). However, Cr-Cr distances come close to 2.3 Å several times during the run, characteristic of a symmetric structure. Compared to the gas phase results at the same temperature (300 K), which feature predominantly symmetric structures, the complexes in the unit cell are mainly asymmetric, indicating a possible packing or neighbouring effect as the origin of this difference.

Lastly, the results for  $Cr_3(\text{dpa})_4(\text{NCS})_2$  in the solid unit cell, represented in Figure 4 (top), are similar to the  $CN^-$  case. Mostly asymmetric structures ( $\Delta\text{dist} > 0.15$  Å) are observed in the simulation with the two  $d(\text{Cr-Cr})$  averaging 1.93 and 2.70 Å, respectively (see Table 2). Symmetric structures ( $\Delta\text{dist} < 0.15$  Å) appear occasionally in the simulation as part of the instantaneous switch between the two possible arrangements.

The average distances and angles extracted from the  $NCS^-$  dynamics are reported in Table 2. In both the symmetric and asymmetric structures the axial Cr-NCS distances are increased in average compared to the gas simulation. This could be the effect of intermolecular interactions in the cell, a side view of which is shown

in Figure 5. Such interactions increase the torsion of the  $NCS^-$  ligand with respect to the Cr chain and make them persistent, in contrast to the occasional appearance in the gas phase simulation. The larger X-Cr distances and the (slightly) increased torsion weaken the  $\sigma$ -donation of the ligand towards the metal chain, favoring asymmetric  $Cr_3$  structures.

It is important to note that the predominantly asymmetric structures obtained with axial  $CN^-$  are not in agreement with the experimental symmetric structure. This discrepancy could be attributed to an overestimation of the neighboring interactions in the calculations, which results in an increased ligand-metal separation and torsion. Also, the flatness of the PES can have a dramatic effect on the outcome of dynamics calculations, in which tiny energy differences, of the order of 1 kcal mol<sup>-1</sup>, can seriously alter the expected trend. Even so, it is clear that neighboring interactions are important and they should be taken into account when comparing experimental (crystal) structures and isolated or even transistor-like environments. We would like to continue studying these effects in more detail by using more advanced wave function methods such as CASSCF/CASPT2.

**Table 1.** Relevant mean distances (d), in Å, and angles (a), in degrees, from the molecular dynamics of Cr<sub>3</sub>(dpa)<sub>4</sub>(NO<sub>3</sub>)<sub>2</sub>. X-ray values are shown. Previous DFT optimized structure shown for comparison.

	Gas phase MD	Crystal MD	X-ray <sup>2</sup>	Static DFT Opt <sup>20</sup>
d(Cr <sub>1</sub> -Cr <sub>2</sub> )	1.942 ± 0.017	1.772 ± 0.053	1.933	2.330
d(Cr <sub>2</sub> ...Cr <sub>3</sub> )	2.622 ± 0.034	2.662 ± 0.061	2.644	2.330
d(X-Cr <sub>1</sub> )	2.418 ± 0.219	2.336 ± 0.399	2.298	2.140
d(X-Cr <sub>3</sub> )	2.192 ± 0.093	2.180 ± 0.112	2.086	2.140
a(N-O-Cr <sub>1</sub> )	152.6 ± 8.3	149.4 ± 10.2	164.7	180.0
a(N-O-Cr <sub>3</sub> )	143.5 ± 9.0	133.6 ± 8.0	129.0	180.0

**Table 2.** Relevant mean distances (d), in Å, and angles (a), in degrees, from the molecular dynamics of Cr<sub>3</sub>(dpa)<sub>4</sub>(NCS)<sub>2</sub>. Average values are reported for the group of symmetric ( $\Delta\text{dist} < 0.15$  Å) and asymmetric ( $\Delta\text{dist} > 0.15$  Å) structures. X-ray values are shown. Previous DFT optimized structure shown for comparison.

	Gas phase MD		Crystal MD		X-ray	Static DFT Opt <sup>20</sup>
	Symmetric	Asymmetric	Symmetric	Asymmetric		
d(Cr <sub>1</sub> -Cr <sub>2</sub> )	2.321	2.268	2.358	1.928	2.234	2.369
d(Cr <sub>2</sub> -Cr <sub>3</sub> )	2.323	2.547	2.379	2.695	2.482	2.369
d(X-Cr <sub>1</sub> )	2.180	2.178	2.363	2.483	2.203	2.105
d(X-Cr <sub>3</sub> )	2.180	2.123	2.195	2.320	2.203	2.105
a(C-N-Cr <sub>1</sub> )	154.7	156.3	145.3	145.6	156.4	180.0
a(C-N-Cr <sub>3</sub> )	154.7	156.5	139.7	147.6	156.4	180.0

## Conclusions

Previously reported static ab initio calculations showed a rather small energy difference between symmetric and asymmetric forms at T = 0 K. The present molecular dynamics study has shown that temperature enhances the asymmetry of the Cr<sub>3</sub> backbone and provides a more detailed knowledge of the different aspects affecting EMACs' geometries. The structure with NO<sub>3</sub><sup>-</sup> axial ligands, already close to being asymmetric in the static calculations, appears as fully asymmetric along the whole time trajectory. On the other hand, the stronger  $\sigma$ -donors CN<sup>-</sup> and NCS<sup>-</sup> give symmetric forms in the gas phase, although a substantial fraction of asymmetric structures appears at room temperature. It can be inferred that the entropic term in the free energy is larger for the asymmetric form, yet we were not able to quantify it due to the impossibility to determine an asymmetric minimum on the PES.

The asymmetry becomes even more pronounced when, in addition to the thermal energy effects, intermolecular interactions in the crystal phase are accounted for. These push the axial ligands away from the Cr<sub>3</sub> axis to allow a more compact crystalline packing, reducing the effectiveness of the axial  $\sigma$ -donation and, consequently, enhancing the prevalence of

distorted (asymmetric) structures. The poor electron donating character of the axial ligands originates the asymmetry, but the key factor is the Cr<sub>3</sub> chain being electron deficient itself. Thus, to reduce the repulsion between the Cr cations in these electron-deficient chains two phenomena can take place: (i) accumulation of electron density between two metal centers by formation of multiple covalent bonds (short Cr-Cr distance), and (ii) distancing of neighboring metal centers (long Cr-Cr distance). All in all, the interactions between molecules in the solid could explain the differences between experimentally assigned and computationally calculated structures. However, it is important to consider that these packing effects might not be present in all technological applications of EMACs, for example in single molecule transistor devices.

## Acknowledgements

Financial support has been provided by the Spanish Administration (CdG, XL, MS Project CTQ2014-51938-P), the Generalitat de Catalunya (CdG, Projects 2014SGR199 and Xarxa d'R+D+I en Química Teòrica i Computacional, XRQTC) and the European Union (CdG, COST Action ECOST-Bio CM1305). We also thank the EPSRC for financial support (VA, EP/K021435/1).

## References

- 1 V. P. Georgiev, P. J. Mohan, D. DeBrincat and J. E. McGrady, *Coord. Chem. Rev.*, 2013, **257**, 290–298.
- 2 S.-Y. Lin, I. W. P. Chen, C. Chen, M.-H. Hsieh, C.-Y. Yeh, T.-W. Lin, Y.-H. Chen and S.-M. Peng, *J. Phys. Chem. B*, 2004, **108**, 959–964.
- 3 D. W. Brogden, Y. Turov, M. Nippe, G. Li Manni, E. A. Hillard, R. Clérac, L. Gagliardi and J. F. Berry, *Inorg. Chem.*, 2014, **53**, 4777–4790.
- 4 R. Clérac, F. A. Cotton, L. M. Daniels, K. R. Dunbar, C. A. Murillo and I. Pascual, *Inorg. Chem.*, 2000, **39**, 748–751.
- 5 M. Nippe and J. F. Berry, *J. Am. Chem. Soc.*, 2007, **129**, 12684–12685.
- 6 M. Nippe, E. Victor and J. F. Berry, *Eur. J. Inorg. Chem.*, 2008, **2008**, 5569–5572.
- 7 M. Nippe, E. Bill and J. F. Berry, *Inorg. Chem.*, 2011, **50**, 7650–7661.
- 8 S.-A. Hua, M.-C. Cheng, C. Chen and S.-M. Peng, *Eur. J. Inorg. Chem.*, 2015, **2015**, 2510–2523.
- 9 S. M. Peng, C. C. Wang, Y. L. Jang, Y. H. Chen, F. Y. Li, C. Y. Mou and M. K. Leung, *J. Magn. Magn. Mater.*, 2000, **209**, 80–83.
- 10 D. Aydin-Cantürk and H. Nuss, *Zeitschrift für Anorg. und Allg. Chemie*, 2011, **637**, 543–546.
- 11 L. C. Wu, M. K. Thomsen, S. R. Madsen, M. Schmoekel, M. R. V Jorgensen, M. C. Cheng, S. M. Peng, Y. S. Chen, J. Overgaard and B. B. Iversen, *Inorg. Chem.*, 2014, **53**, 12489–12498.
- 12 J. P. Malrieu, R. Caballol, C. J. Calzado, C. de Graaf and N. Guihéry, *Chem. Rev.*, 2014, **114**, 429–492.
- 13 S.-H. Lai, C.-J. Hsiao, J.-W. Ling, W.-Z. Wang, S.-M. Peng and I.-C. Chen, *Chem. Phys. Lett.*, 2008, **456**, 181–185.
- 14 Z. Tabookht, X. López and C. de Graaf, *J. Phys. Chem. A*, 2010, **114**, 2028–2037.
- 15 Z. Tabookht, X. López, M. Bénard and C. de Graaf, *J. Phys. Chem. A*, 2010, **114**, 12291–12298.
- 16 Z. Tabookht, C. de Graaf and X. López, *Dalt. Trans.*, 2012, **41**, 498–504.
- 17 M. Nippe, Y. Turov and J. F. Berry, *Inorg. Chem.*, 2011, **50**, 10592–10599.
- 18 J. F. Berry, F. A. Cotton, T. Lu, C. A. Murillo, B. K. Roberts and X. Wang, *J. Am. Chem. Soc.*, 2004, **126**, 7082–7096.
- 19 C.-J. Hsiao, S.-H. Lai, I. C. Chen, W.-Z. Wang and S.-M. Peng, *J. Phys. Chem. A*, 2008, **112**, 13528–13534.
- 20 M. Spivak, V. Arcisauskaitė, X. Lopez, J. E. McGrady and C. de Graaf, *Dalt. Trans.*, 2017, **46**, 6202–6211.
- 21 V. Arcisauskaitė, M. Spivak and J. E. McGrady, *Inorganica Chim. Acta*, 2015, **424**, 293–299.
- 22 V. P. Georgiev and J. E. McGrady, *J. Am. Chem. Soc.*, 2011, **133**, 12590–12599.
- 23 K. Andersson, P. A. Malmqvist, B. O. Roos, A. J. Sadlej and K. Wolinski, *J. Phys. Chem.*, 1990, **94**, 5483–5488.
- 24 K. Andersson, P. Malmqvist and B. O. Roos, *J. Chem. Phys.*, 1992, **96**, 1218–1226.
- 25 P. G. Szalay, T. Müller, G. Gidofalvi, H. Lischka and R. Shepard, *Chem. Rev.*, 2012, **112**, 108–181.
- 26 R. Car and M. Parrinello, *Phys. Rev. Lett.*, 1985, **55**, 2471–2474.
- 27 <http://www.cpmd.org/>, Copyright IBM Corp 1990–2008, Copyright MPI für Festkörperforschung Stuttgart 1997–2001.
- 28 A. D. Becke, *Phys. Rev. A*, 1988, **38**, 3098–3100.
- 29 C. Lee, W. Yang and R. G. Parr, *Phys. Rev. B*, 1988, **37**, 785–789.
- 30 N. Troullier and J. L. Martins, *Phys. Rev. B*, 1991, **43**, 1993–2006.
- 31 S. Nosé, *J. Chem. Phys.*, 1984, **81**, 511–519.
- 32 S. Nosé, *Mol. Phys.*, 1984, **52**, 255–268.
- 33 W. G. Hoover, *Phys. Rev. A*, 1985, **31**, 1695–1697.
- 34 R. N. Barnett and U. Landman, *Phys. Rev. B*, 1993, **48**, 2081–2097.
- 35 G. Kresse and J. Hafner, *Phys. Rev. B*, 1993, **47**, 558–561.
- 36 G. Kresse and J. Hafner, *Phys. Rev. B*, 1994, **49**, 14251–14269.
- 37 G. Kresse and J. Furthmüller, *Comput. Mater. Sci.*, 1996, **6**, 15–50.
- 38 G. Kresse and J. Hafner, *J. Phys. Condens. Matter*, 1994, **6**, 8245.
- 39 G. Kresse and D. Joubert, *Phys. Rev. B*, 1999, **59**, 1758–1775.
- 40 J. P. Perdew, K. Burke and M. Ernzerhof, *Phys. Rev. Lett.*, 1996, **77**, 3865–3868.

